Estimation of Resolution and Covariance of Ambient Seismic Source Distributions: Full Waveform Inversion and Matched Field Processing

Zongbo Xu, T. Dylan Mikesell

JGR Solid Earth

RESEARCH ARTICLE
10.1029/2022JB024374

Estimation of Resolution and Covariance of Ambient Seismic Source Distributions: Full Waveform Inversion and Matched Field Processing

Zongbo Xu[1] **and T. Dylan Mikesell**[2]

[1]Université Paris Cité, Institut de Physique du Globe de Paris, CNRS, Paris, France, [2]Norwegian Geotechnical Institute, Oslo, Norway

Key Points:

- We present the model resolution and point spread function for two ambient seismic source estimation methods, FWI and MFP
- We demonstrate that with enough independent data, FWI possesses higher resolution than MFP
- We quantify the model covariance of FWI to provide the source strength trade-offs

Correspondence to:
Z. Xu,
zongboxu@ipgp.fr

Citation:
Xu, Z., & Mikesell, T. D. (2022). Estimation of resolution and covariance of ambient seismic source distributions: Full waveform inversion and matched field processing. *Journal of Geophysical Research: Solid Earth*, *127*, e2022JB024374. https://doi.org/10.1029/2022JB024374

Received 13 MAR 2022
Accepted 20 MAY 2022

Abstract Both natural and anthropogenic seismic sources generate so-called ambient seismic waves. One in turn can use ambient seismic waves to estimate these source distributions and study source characteristics, for instance the source mechanism. A commonly used estimation method is called matched field processing (MFP), and the MFP results are inherently smeared by the array geometry. Another approach to estimate ambient seismic sources is to apply full waveform inversion (FWI) to the crosscorrelations of ambient seismic wave recordings. Both methods have pros and cons, but the model resolution and uncertainty in these two methods are important for the interpretation. Unfortunately, this topic has attracted little attention in the past. We propose to estimate both the model resolution matrix and model covariance matrix of the inversion using singular value decomposition. We demonstrate our estimates using two examples, one of which is an actual field array geometry. We quantitatively compare the model resolution of the two methods and discuss the model null space. We demonstrate that FWI has superior resolution with enough independent data and should be used when computational resources permit.

Plain Language Summary Many natural phenomena (such as ocean waves due to a hurricane or glacier tremor due to subglacial water flow) can shake the ground and generate seismic waves. By studying the seismic waves, we can image these natural phenomena in space and monitor the temporal evolution of these phenomena. We focus on two common methods to image these passive sources: matched field processing (MFP) and full waveform inversion (FWI). The resolution and uncertainties of these two methods are important for interpreting imaging results. Thus, we derive and calculate the model resolution for each method. We also study the model trade-off of full waveform inversion to quantify the uncertainty in the inversion results. We compare the resolution of the two methods using a realistic field seismic array form a past experiment. We show that FWI has better resolution than MFP when all seismic sensors in the array are used, indicating that FWI should be the preferred method for ambient noise source imaging when computational resources permit its use.

1. Introduction

Many natural phenomena can generate seismic waves, such as CO_2 fumaroles (e.g., Estrella et al., 2016; Umlauft & Korn, 2019), landslides (e.g., Brodsky et al., 2003), rivers (e.g., Roth et al., 2014; Tsai et al., 2012), and ocean waves (e.g., Hasselmann, 1963; Longuet-Higgins, 1950). Surface waves usually dominate the seismic recordings on the Earth's surface. We refer to these seismic recordings as ambient seismic recordings and the seismic sources as ambient seismic sources. In the ambient seismic recordings, there are commonly no clear body-wave arrivals as in earthquake recordings. Ambient seismic recordings are used to infer information about the corresponding ambient seismic sources. For example, based on the ambient seismic waves (i.e., microseism) generated by ocean wave coupling with the seafloor, one can estimate the coupling distribution (e.g., Ermert et al., 2017; Juretzek & Hadziioannou, 2016), monitor the spatial and temporal changes of the source distributions (e.g., Gal et al., 2018; Retailleau & Gualtieri, 2019), study how environmental changes affect the source strength (e.g., Grob et al., 2011), and investigate the source mechanism (e.g., Ardhuin et al., 2015; Gualtieri et al., 2020; Nishida et al., 2008).

One often estimates the spatial ambient seismic source distributions (strength and location) when studying ambient seismic sources. One can image source locations using traditional imaging methods without expensive computation [e.g., matched-field processing (MFP), Baggeroer et al., 1988; Bucker, 1976], for example, to

investigate glacier tremors (e.g., Umlauft et al., 2021) or the hydrothermal system at Old Faithful Geyser (e.g., Cros et al., 2011). In using MFP, one crosscorrelates ambient seismic recordings to extract coherent signals and then apply backprojection to the crosscorrelations to image the source locations (e.g., Cros et al., 2011). Note that the MFP results are not the true source strength distributions and also include seismic array artifacts (we demonstrate this in Section 2.4). In contrast, one can estimate both the source locations and strengths by applying full-waveform inversion to the same crosscorrelations (e.g., Fichtner et al., 2017; Hanasoge, 2014; Tromp et al., 2010). This inversion method has been applied to both low- (<0.2 Hz) and high-frequency (>2 Hz) ambient seismic waves (e.g., Ermert et al., 2017; Xu et al., 2020, respectively). The two source imaging methods share some similarities (e.g., Bowden et al., 2021). For example, Xu et al. (2020) demonstrate that MFP can be written as the crosscorrelation waveform inversion sensitivity kernel with zero initial sources, and both methods require a subsurface velocity model as an input. In this paper, we refer to the full-waveform inversion for ambient seismic sources as source inversion. We detail the link between source inversion and MFP in Section 2.4.

Assessing estimates of ambient seismic source distributions in terms of uncertainty is necessary but has not been fully studied. Source inversion results can be biased by the subsurface model, for instance due to inaccurate velocities (e.g., Xu et al., 2019) or anelasticity (e.g., Xu et al., 2020). Besides biases, source inversion has different sensitivities to seismic sources at different locations simply due to the array geometry (e.g., Burtin et al., 2010; Datta et al., 2019). Thus, assessing the model resolution and uncertainty (i.e., covariance) will aid interpretation of source inversion results. To estimate the model resolution, similar to seismic tomography studies, one can adopt synthetic reconstruction tests like the spike test (e.g., Ermert et al., 2017). In the spike test, one sets one or multiple spike(s) inside or outside the array as the true model and generates synthetic data from the source model; one then applies the source inversion to the synthetic data to check how the inversion recovers the spike(s). A similar test can be adopted in MFP (e.g., Gal et al., 2018). It is computationally expensive to assess the resolution for each source location, as one needs to conduct the spike test at all the source locations, bearing in mind that the sensitivity at one spike location can change due to other spikes existing simultaneously (e.g., Xu et al., 2020). Another commonly used test in seismic tomography studies, the checkerboard test, has not yet been studied in source inversion, perhaps because the checkerboard-like models do not represent plausible heterogeneous source distributions. In this source inversion study, we analyze the source distribution uncertainty under the assumption that the subsurface structure is known. It is critical to note that a trade-off exists between the source and the structure (Fichtner, 2014; Sager et al., 2018), and thus an inaccurate structure model leads to another type of the source uncertainty, which we do not consider here. This trade-off is an inherent obstacle in the ambient noise source inversion problem and deserves further research. However, first we should understand each uncertainty individually.

To calculate the model resolution efficiently, we frame source inversion as a linear inversion problem using a waveform misfit function. Given that singular value decomposition (SVD) is commonly used to estimate linear-inversion model resolution (e.g., in tomography studies, Aster et al., 2012), we propose to calculate the model resolution using SVD. We also present the model resolution of MFP theoretically. Within this frame work, we calculate the model covariance matrix of source inversion (Section 2). We then demonstrate our estimation of the model resolution and covariance through two array examples (Section 3), where we compare the model resolution of source inversion to MFP in a field array geometry. Lastly, we assess application of winnowing data to our calculation and discuss the model null space in all these methods (Section 4).

2. Estimation of the Model Resolution and Covariance

For source inversion, we calculate the model resolution matrix and covariance matrix using singular value decomposition (Section 2.1 and 2.2). We then demonstrate that framing source inversion as a nonlinear inversion problem provides the same model covariance matrix as the linear source inversion (Section 2.3). We also apply SVD to MFP to provide the model resolution, and we demonstrate that the MFP result includes the array information (Section 2.4).

2.1. The Linear Source Inversion

We frame the source inversion as a classic linear inversion problem (which we refer to as the linear source inversion) because a crosscorrelation between two seismic sensors can be written as

$$C\left(r_m, r_n, \omega\right) = \sum_{q=1}^{Q} G\left(r_m, s_q, \omega\right) G^*\left(r_n, s_q, \omega\right) N\left(s_q, \omega\right), \tag{1}$$

where r_m (r_n) is the mth (nth) sensor location, ω is the angular frequency, $G(r_m, s_q)$ is the Green's function for a seismic source at s_q and a sensor r_m, * denotes the complex conjugate, $N(s_q)$ is the ambient seismic source strength at s_q. $N(s_q)$ is the autocorrelation of the source wavelet and thus is a non-negative real value (e.g., Wapenaar & Fokkema, 2006). Q is the total number of the sources. Here, we assume that the seismic sources are independent from each other and the subsurface structure is known. Note that the two assumptions may not be valid in practice (e.g., Ayala-Garcia et al., 2021; Xu et al., 2020). We write the above equation for M stations (i.e., r_1, r_2,…,r_M) in matrix form as

$$\begin{bmatrix} C\left(r_1, r_2\right) \\ C\left(r_1, r_3\right) \\ \vdots \\ C\left(r_2, r_3\right) \\ \vdots \\ C\left(r_{M-1}, r_M\right) \end{bmatrix} = \begin{bmatrix} G\left(r_1, s_1\right) G^*\left(r_2, s_1\right) & G\left(r_1, s_2\right) G^*\left(r_2, s_2\right) & \dots & G\left(r_1, s_Q\right) G^*\left(r_2, s_Q\right) \\ G\left(r_1, s_1\right) G^*\left(r_3, s_1\right) & G\left(r_1, s_2\right) G^*\left(r_3, s_2\right) & \dots & G\left(r_1, s_Q\right) G^*\left(r_3, s_Q\right) \\ \vdots & \vdots & \vdots & \vdots \\ G\left(r_2, s_1\right) G^*\left(r_3, s_1\right) & G\left(r_2, s_2\right) G^*\left(r_3, s_2\right) & \dots & G\left(r_2, s_Q\right) G^*\left(r_3, s_Q\right) \\ \vdots & \vdots & \vdots & \vdots \\ G\left(r_{M-1}, s_1\right) G^*\left(r_M, s_1\right) & G\left(r_{M-1}, s_2\right) G^*\left(r_M, s_2\right) & \dots & G\left(r_{M-1}, s_Q\right) G^*\left(r_M, s_Q\right) \end{bmatrix} \begin{bmatrix} N\left(s_1\right) \\ N\left(s_2\right) \\ \vdots \\ N\left(s_Q\right) \end{bmatrix}, \tag{2}$$

where we omit ω for brevity. Note that in this study, we focus on a single frequency to demonstrate our analysis, while in practice one will use multiple frequencies for source inversion. In the following, we use normal symbols to refer to scalars, and we use lower-case bold and upper-case bold symbols to refer to vectors and matrices, respectively.

We recognize that Equation 2 is a classic linear inversion problem ($\mathbf{b} = \mathbf{A}\mathbf{x}$) with.

$$b_p = C\left(r_m, r_n\right), \tag{3a}$$

$$x_q = N\left(s_q\right), \tag{3b}$$

$$A_{pq} = G\left(r_m, s_q\right) G^*\left(r_n, s_q\right), \tag{3c}$$

where p is the index for the sensor pair, r_m and r_n. $\mathbf{A}$ is a P-by-Q matrix and $P = M(M-1)/2$ for M sensors. Each element in $\mathbf{A}$ is a crosscorrelation between the Green's functions for two sensors to one common source (Equation 3c). When calculating the Green's function values, we can use analytical Green's functions or the results from a wave equation solver. In addition, although we do not study it here, one can use the different components of the Green's tensors (e.g., vertical-vertical or radial-vertical). We use two stations to illustrate $\mathbf{A}$ in Section 3.1. Note that in Equation 2, we do not consider any commonly used pre-processing procedures for ambient seismic recordings like time-/frequency-domain normalization (e.g., Bensen et al., 2007). One could incorporate the procedures into the linear inversion with matrix multiplication or vector addition (e.g., Fichtner et al., 2020). We assess another commonly used ambient seismic data processing, winnowing crosscorrelations, in Section 4.1.

One can use singular value decomposition (SVD) to analyze linear inversion problems, for example, calculation of the model resolution. We apply SVD to $\mathbf{A}$ as

$$\mathbf{A} = \mathbf{U}\mathbf{S}\mathbf{V}^{\dagger}, \tag{4}$$

where $\mathbf{V}^{\dagger} = (\mathbf{V}^{*})^{T}$ and T represents the matrix transpose. While SVD for real matrices only involves matrix transpose, the SVD here involves the conjugate transpose operation because $\mathbf{A}$ is complex-valued. $\mathbf{U}$ and $\mathbf{V}$ are P-by-P and Q-by-Q matrices, respectively. The columns in $\mathbf{U}$ and $\mathbf{V}$ are orthogonal bases for the whole data space and whole model space, respectively. $\mathbf{S}$ is a diagonal matrix and the diagonal elements are singular values. The singular values here are non-negative and real. Singular values generally indicate how a linear inversion constrains the corresponding model-space base vectors. For example, a larger absolute singular value in the qth column of $\mathbf{S}$ means that the qth column vector in $\mathbf{V}$ is better constrained and is less affected by data noise (e.g., Aster et al., 2012).

Ideally for a linear inversion problem, we would like to have more linearly independent data than unknown model parameters. Thus, the inversion can constrain the whole model space, which means we can recover the true model. However in practice, as in source inversion, we usually have many more parameters than data, that is, $Q > P$. If we assume $\mathbf{A}$ is a full-row-rank matrix, we only have non-zero singular values for the first P columns of $\mathbf{V}$ ($\mathbf{V}_P$). Thus, we can only use those columns in constructing a solution using the linear inversion methods (e.g., pseudoinverse and zeroth-order Tikhonov regularization) or using some nonlinear inversion algorithms (Section 2.3). The vectors in $\mathbf{V}_P$ construct a subspace in the model space, and this subspace is usually referred to as the row space in linear algebra (e.g., Strang, 2016). We state that $\mathbf{V}_P$ spans the row space, which means that any vector in this space is a linear combination of the vectors in $\mathbf{V}_P$. For the $Q - P$ columns left in $\mathbf{V}$, these column vectors are orthogonal to the vectors in $\mathbf{V}_P$. Thus any linear combination of the $Q - P$ columns is also orthogonal to the row space and cannot be resolved by the linear inversion. The space spanned by the $Q - P$ vectors is the model null space. We discuss this space further in Section 4.2.

2.2. Model Resolution and Covariance

One uses $\mathbf{V}_P$ to calculate the model resolution for a linear inversion problem as

$$\mathbf{R}_{\mathbf{m}} = \mathbf{V}_P\mathbf{V}_P^{\dagger}, \tag{5}$$

where $\mathbf{R}_{\mathbf{m}}$ is conventionally called as the model resolution matrix (e.g., Aster et al., 2012). The maximum real value in $\mathbf{R}_{\mathbf{m}}$ can be up to 1. Note that in the linear inversion theory, $\mathbf{R}_{\mathbf{m}}$ links the estimated model ($\mathbf{x}^e$) and true model ($\mathbf{x}^t$) as

$$\mathbf{x}^e = \mathbf{R}_{\mathbf{m}}\mathbf{x}^t. \tag{6}$$

One can think of $\mathbf{R}_{\mathbf{m}}$ as smearing the true model. We notice that if $\mathbf{x}^t = 0$ except the qth component (i.e., $x_q^t = 1$), $\mathbf{x}^e$ would be the qth column of $\mathbf{R}_{\mathbf{m}}$ and also the response for the qth model parameter. Thus, the columns in $\mathbf{R}_{\mathbf{m}}$ are the point spread functions for the individual model parameters. If $\mathbf{A}$ is a full-rank square matrix, $\mathbf{R}_{\mathbf{m}}$ would be an identity matrix and the point spread function becomes a delta function, where $\mathbf{x}^e$ and $\mathbf{x}^t$ would be the same. However due to the rank deficiency of $\mathbf{A}$ in practice, $\mathbf{R}_{\mathbf{m}}$ is not an identity matrix. If the diagonal elements of $\mathbf{R}_{\mathbf{m}}$ are closer to 1, the point spread functions are also closer to the delta functions, and thus, the model parameters are well resolved. Therefore, the diagonal elements of $\mathbf{R}_{\mathbf{m}}$ represent the resolution for the model parameters, that is, the source strengths here (N in Equation 2). Note that our calculation of the model resolution is similar to Meyers et al. (2021) where they image the resolution for seismic source angular distributions. We present not only the resolution but also the point spread functions for the source strengths (Section 3).

Besides the model resolution one also uses $\mathbf{V}_P$ and $\mathbf{S}$ to calculate the model covariance matrix for the inversion results as

$$\mathbf{C}_{\mathbf{m}} = \sigma^2\left(\mathbf{A}^{\dagger}\mathbf{A}\right)^{-1} = \sigma^2\mathbf{V}_P\mathbf{S}_P^{-2}\mathbf{V}_P^{\dagger}, \tag{7}$$

where σ is the data error and $\mathbf{S}_P$ is the first P columns of $\mathbf{S}$. One commonly uses the square root of the diagonal elements in $\mathbf{C}_{\mathbf{m}}$ to calculate the confidence intervals or uncertainties for the model parameters; the off-diagonal elements represent the trade-off among the different model parameters (e.g., Aster et al., 2012). Note that compared to the model resolution (Equation 5), an extra term, $\mathbf{S}_P^{-2}$, exists in the model covariance matrix

(Equation 7). Due to this term, the maximum values for the model covariance matrix can be much larger than 1 (Section 3.2). Here, we assume that the data errors are independent and constant among all crosscorrelations, and thus, we set $\sigma = 1$ in the following examples for simplicity. Note that one could incorporate the data error into source inversion, especially in practice (Section 4.4). We use the real values of $\mathbf{R_m}$ and $\mathbf{C_m}$ since our model parameters are real-valued. We illustrate estimation of the model resolution and covariance through the examples in Section 3.

2.3. Nonlinear Source Inversion

One commonly applies nonlinear inversion algorithms, instead of linear inversion algorithms, to source inversion (which we refer to as the nonlinear source inversion). When using the nonlinear source inversion, one can constrain the solutions to be non-negative (i.e., seismic source strength, N in Equation 1). One can also use the nonlinear source inversion to focus on not only the spectra/waveform of the crosscorrelations (Equation 1) but also other properties of the crosscorrelations such as the envelope (Bozdağ et al., 2011; Fichtner et al., 2008) or the energy balance (i.e., the symmetry, Ermert et al., 2015) because these properties possess different sensitivities to the seismic sources than the waveform (e.g., Sager et al., 2018).

In the nonlinear source inversion, one defines a misfit function (χ) to measure the misfit between the observed (C^o) and synthetic (C) crosscorrelations, where the synthetic data are based on a trial solution. For example, one often uses the L_2-norm waveform misfit function written as:

$$\chi(\omega) = \frac{1}{2}\sum_{m,n}\left\|C\left(r_m, r_n, \omega\right) - C^o\left(r_m, r_n, \omega\right)\right\|_2^2, \tag{8}$$

$$= \frac{1}{2}\left(\mathbf{Ax} - \mathbf{b}^o\right)^\dagger\left(\mathbf{Ax} - \mathbf{b}^o\right), \tag{9}$$

where $\mathbf{b}^o$ is the observed data vector. Note that the solutions for Equation 9 are the same as for the linear source inversion (e.g., Menke, 2012), Equations 1 and 2. To minimize the waveform misfit function, we write the gradient as

$$\nabla\chi = \mathbf{J}^\dagger\left(\mathbf{Ax} - \mathbf{b}^o\right), \tag{10}$$

where $\mathbf{J}$ is the Jacobian matrix (e.g., Aster et al., 2012). Here, $\mathbf{J}$ is written as

$$\begin{bmatrix} \frac{\partial C(r_1,r_2)}{\partial N(s_1)} & \frac{\partial C(r_1,r_2)}{\partial N(s_2)} & \cdots & \frac{\partial C(r_1,r_2)}{\partial N(s_Q)} \\ \frac{\partial C(r_1,r_3)}{\partial N(s_1)} & \frac{\partial C(r_1,r_3)}{\partial N(s_2)} & \cdots & \frac{\partial C(r_1,r_3)}{\partial N(s_Q)} \\ \vdots & \vdots & \vdots & \vdots \\ \frac{\partial C(r_2,r_3)}{\partial N(s_1)} & \frac{\partial C(r_2,r_3)}{\partial N(s_2)} & \cdots & \frac{\partial C(r_2,r_3)}{\partial N(s_Q)} \\ \vdots & \vdots & \vdots & \vdots \\ \frac{\partial C(r_{M-1},r_M)}{\partial N(s_1)} & \frac{\partial C(r_{M-1},r_M)}{\partial N(s_2)} & \cdots & \frac{\partial C(r_{M-1},r_M)}{\partial N(s_Q)} \end{bmatrix}, \tag{11}$$

where $\frac{\partial C(r_1,r_2)}{\partial N(s_1)}$ is the partial derivative of the crosscorrelation, $C(r_1, r_2)$, with respect to the source strength, $N(s_1)$. Based on Equation 1, we recognize that $\frac{\partial C(r_1,r_2)}{\partial N(s_1)} = G\left(r_1, s_1\right)G^*\left(r_2, s_1\right)$ and the Jacobian matrix is $\mathbf{A}$. Note that one can estimate the model covariance for the nonlinear inversion problems using the Jacobian matrix, as $\mathbf{C_m} = \left(\mathbf{J}^\dagger\mathbf{J}\right)^{-1}$ (e.g., Aster et al., 2012). Since $\mathbf{J} = \mathbf{A}$ here, the covariance formula becomes $\left(\mathbf{A}^\dagger\mathbf{A}\right)^{-1}$, the model covariance for the linear inversion (Equation 7). Note that in practice one commonly adopts regularization in the nonlinear source inversion (e.g., spatially smoothing the source strengths, Ermert et al., 2017; Sager et al., 2018). The regularization leads to changes in the misfit functions and thus a different covariance. This topic is interesting but beyond the scope of this study.

To examine the links (e.g., the SVD, the row space, and the null space) between nonlinear and linear source inversion, we analyze gradient descent algorithm, commonly used in nonlinear source inversion. We note that one

could do the same analysis with other nonlinear inversion methods. When using gradient descent, one updates a trial solution iteratively as

$$\mathbf{x}^{l+1} = \mathbf{x}^{l} - \alpha \nabla \chi^{l}, \tag{12}$$

where $\nabla\chi^l$ is the gradient for the solution at the lth iteration ($\mathbf{x}^l$) and α is the step length. For the waveform misfit function (Equation 9), the gradient is Equation 10. We rewrite Equation 10 using the SVD results as

$$\nabla \chi = \sum_{p=1}^{P} \left[\mathbf{u}_p^{\dagger} (\mathbf{b} - \mathbf{b}^{o}) S_p\right] \mathbf{v}_p, \tag{13}$$

where $\mathbf{b}$ is the synthetic data vector and S_p is the pth singular value; $\mathbf{u}_p$ and $\mathbf{v}_p$ are the pth columns in $\mathbf{U}$ and $\mathbf{V}$, respectively. We observe that the gradient is a linear combination of the vectors in $\mathbf{V}_P$. Thus, the gradient is in the row space. This implies that if the initial model is in the row space, the gradient-descent algorithm should also converge to a solution in the row space. Note that our analysis in this section is based on the L_2-norm misfit function (Equation 9). For other types of misfit functions (e.g., envelope or the energy balance), one would need to use the corresponding Jacobian or Hessian matrix for the uncertainty analysis (e.g., Fichtner & Trampert, 2011a; Sager et al., 2018).

2.4. Matched-Field Processing

We compare MFP to source inversion. We write the formula for MFP (e.g., Cros et al., 2011) using consistent notation as

$$y(s_q, \omega) = \sum_{m,n} G^{*}(r_m, s_q, \omega)\, G(r_n, s_q, \omega)\, C(r_m, r_n, \omega), \tag{14}$$

and in the vector-matrix format as

$$\mathbf{y} = \mathbf{A}^{\dagger}\mathbf{b}, \tag{15}$$

where $y(s_q, \omega)$ and $\mathbf{y}$ are the MFP estimates. Note that the MFP estimate includes the array information ($\mathbf{A}^{\dagger}$) because $\mathbf{A}$ includes the Green's functions for all the station locations in an array. Thus, $\mathbf{y}$ is not the source strengths as in source inversion (i.e., $\mathbf{x}$). Using $\mathbf{A}\mathbf{x}^t = \mathbf{b}$ where $\mathbf{x}^t$ is the true solution, we rewrite Equation 15 as.

$$\mathbf{y} = \mathbf{A}^{\dagger}\mathbf{A}\mathbf{x}^{t}, \tag{16}$$

$$= \mathbf{V}_P \mathbf{S}_P^2 \mathbf{V}_P^{\dagger} \mathbf{x}^{t}, \tag{17}$$

$$= \sum_{p=1}^{P} S_p^2 \left(\mathbf{v}_p^{\dagger}\mathbf{x}^{t}\right) \mathbf{v}_p, \tag{18}$$

where $\mathbf{S}_P$ (S_p) and $\mathbf{V}_P$ ($\mathbf{v}_p$) are the same as in source inversion. Note that Equation 18 indicates that the MFP result is a linear combination of the vectors in $\mathbf{V}_P$. Thus, the MFP result is also in the row space of $\mathbf{A}$, as is the gradient of the waveform misfit function in nonlinear source inversion (Equation 13).

We notice that the MFP result is a product between $\mathbf{A}^{\dagger}\mathbf{A}$ (or $\mathbf{V}_P\mathbf{S}_P^2\mathbf{V}_P^{\dagger}$) and the true solution (Equations 16 and 17). Thus, $\mathbf{A}^{\dagger}\mathbf{A}$ converts the true model to the blurry estimate ($\mathbf{y}$ in Equations 16 and 17). As such, each column in $\mathbf{A}^{\dagger}\mathbf{A}$ is the point spread function for the corresponding source. However in contrast to $\mathbf{R}_{\mathbf{m}}$ (i.e., $\mathbf{V}_P\mathbf{V}_P^{\dagger}$), which could be an identity matrix with perfect resolution, $\mathbf{A}^{\dagger}\mathbf{A}$ for MFP cannot be an identity matrix due to $\mathbf{S}_P^2$ in Equation 17, unless all the singular values are 1. Since $\mathbf{A}^{\dagger}\mathbf{A}$ acts as a filter on $\mathbf{x}^t$, we refer to $\mathbf{A}^{\dagger}\mathbf{A}$ (or $\mathbf{V}_P\mathbf{S}_P^2\mathbf{V}_P^{\dagger}$) as MFP filter in the following. The covariance matrix of the MFP estimate is similar to MFP filter (Appendix A), and thus, we only discuss MFP filter in the following.

3. Examples of Model Resolution and Covariance

We present calculation of the model resolution and model covariance for two examples. The first example consists of two stations, where we use this simple geometry to illustrate **A** and application of SVD to **A**. The second example is based on the geometry of the field array presented in Xu et al. (2020). We compute the model resolution of both source inversion and MFP for this array; we also compute the model covariance of source inversion. We demonstrate that these calculations can aid the source inversion. We study Rayleigh waves in the two examples, but the methodology also applies for body waves.

3.1. A Two-Station Example

We place two stations ($M = 2$ and $P = 1$) separated by 2,100 m on the Earth's surface. For the potential source locations around the two stations, we create a source grid, 91 by 91 elements with a 40 m grid distance. We assume that all the sources only emit vertical-direction forces on the surface (i.e., the x-y plane). We also assume that the subsurface medium is elastic, laterally homogeneous, and isotropic. Thus in constructing **A** (Equation 2), we use the vertical-component far-field Rayleigh-wave Green's function

$$G(r,\omega) = \sqrt{\frac{1}{8\pi\omega r/c(\omega)}}\, e^{-i(\omega r/c(\omega)+\pi/4)}, \tag{19}$$

where ω is the angular frequency, r is the Rayleigh-wave propagation distance from the source to the receiver, c is the Rayleigh-wave phase velocity at the frequency ω, and i denotes the imaginary unit. Here, we set $c = 2{,}000$ m/s at 3 Hz. The formula above is derived from a normalization of the full Rayleigh-wave Green's function (Haney et al., 2012) and has units of s^2/kg.

As we only have one sensor pair in this example, **A** is a complex-valued row vector where each element corresponds to a source in the source grid. **A** here represents the contribution of each source location to the two-sensor crosscorrelation. We image the real and imaginary parts of **A** separately based on the source locations in the x–y planes (Figure 1). We observe that the two parts both contain hyperbolic shapes. This is because here all the elements in **A** can be written as $\frac{c}{8\pi\omega\sqrt{r_{1q}r_{2q}}} e^{-i\omega(r_{1q}-r_{2q})/c}$, where r_{1q} is the distance between a source (s_q) and the receiver (r_1). The phase of the exponential, $-\omega(r_{1q} - r_{2q})/c$, is constant when $r_{1q} - r_{2q}$ is constant; a constant $r_{1q} - r_{2q}$ requires s_q to be on a hyperbola with foci at r_1 and r_2. We overlay two types of hyperbolas on the images from formulas $r_{1q} - r_{2q} = 2\pi Ic/\omega$ and $r_{1q} - r_{2q} = (2\pi I - \pi)c/\omega$, where $I = 0, \pm1, \pm2\ldots$. The locations of the maximum and minimum amplitudes are shifted in the two images. In the real part, the maximum amplitudes lie along the first hyperbolas, because the sources along the hyperbolas lead to $e^{-i\omega(r_{1q}-r_{2q})/c} = 1$ (solid curves in Figure 1a); the same logic applies for the minima as the second hyperbola leads to $e^{-i\omega(r_{1q}-r_{2q})/c} = -1$ (dashed curves in Figure 1a). The hyperbolas contribute to real values, but zero to the imaginary part as the curves lie along the nodes in Figure 1b. The real and imaginary parts are actually orthogonal to each other due to the orthogonality of the sine and cosine functions in $e^{-i\omega(r_{1q}-r_{2q})/c}$. Xu et al. (2019) observe a similar phenomenon in the gradient of the nonlinear source inversion with not only the waveform misfit function but also the arrival time misfit function. Note that these hyperbola shape will be a different shape if the subsurface is not laterally homogeneous.

We apply SVD to **A** and achieve **U**, **S**, and **V**. Since we only have one row in **A**, **U** is a scalar, 1. **S** is a row vector and all the elements are zeros except one real value in the first element (S_1). The first column of **V** ($\mathbf{V}_1$) is the only basis vector in the model space spanned by **A** and thus is a scaled version of **A**. Therefore the model resolution, or the diagonal elements of $\mathbf{V}_1\mathbf{V}_1^{\dagger}$, is a scaled version of $\frac{c^2}{64\pi^2\omega^2 r_{1q}r_{2q}}$, the square of the non-exponential part in the elements of **A** (Figure 1c). To confirm this, we plot two model resolution contours crossing two different points (Figure 1c). For each point, we plot another curve across the point and set that $r_{1q}r_{2q}$ on the curve is constant. We observe that the contours overlap with the two curves. Thus, the high model resolution values surrounding the two stations are due to the singularities at the two station locations. The model resolution and the diagonal elements of the covariance matrix are similar (Figures 1c and 1d) because in this case, Equations 5 and 7 are the same but are scaled with 1 and S_1^{-2}, respectively. The MFP filter in this example would be the same as the source-inversion model resolution but is scaled with S_1^2 (Equation 17). Thus, we do not image this MFP filter. We consider the

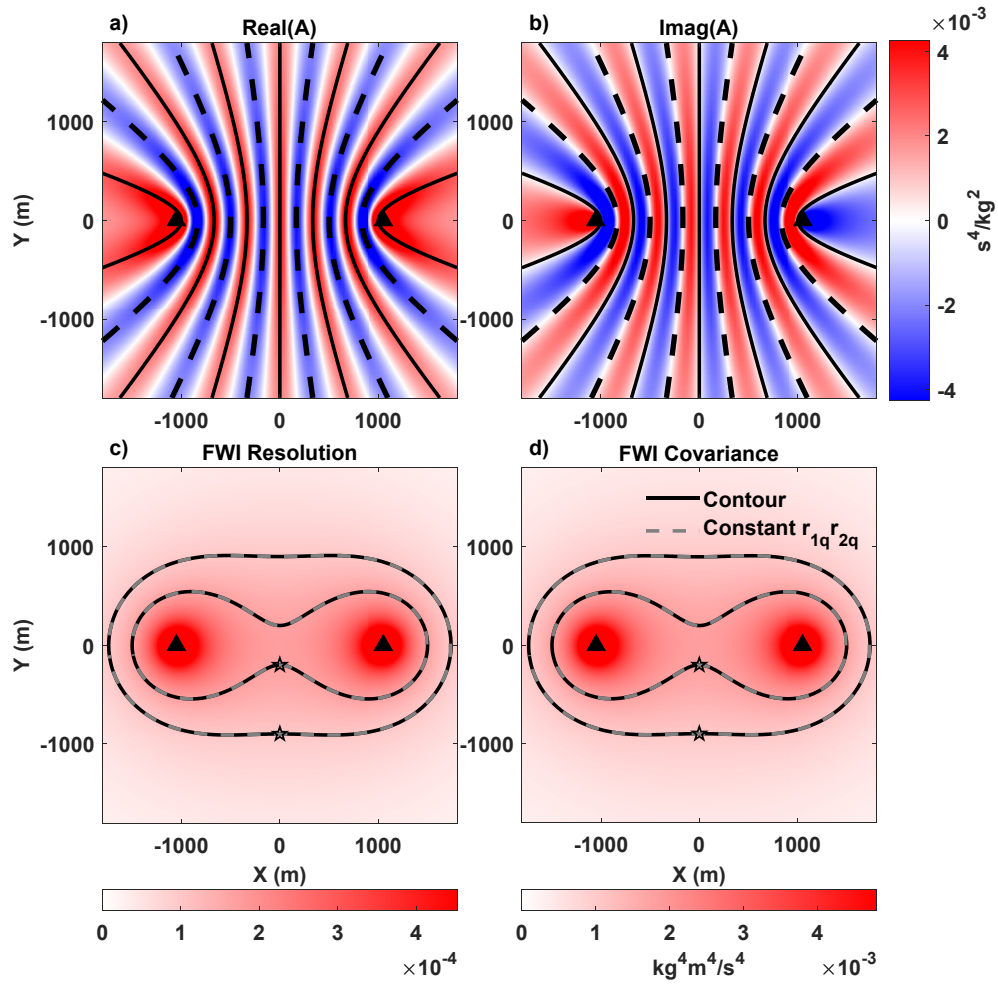

Figure 1. Illustration of the real (a) and imaginary (b) part of **A**, the model resolution (c), and the diagonal elements of the model covariance matrix (d) for the two-station example. The black triangles are the two stations where the stations r_1 and r_2 are located at (−1,050, 0) and at (1,050, 0), respectively. The solid and dashed hyperbolas (a) and (b) represent $r_{1q} - r_{2q} = 2\pi Ic/\omega$ and $(2\pi I - \pi)c/\omega$, respectively. Here, $\omega = 6\pi$ for 3 Hz, $c = 2{,}000$ m/s and $I = 0, \pm 1, \pm 2\ldots$ The black contours (c) and (d) are based on the values at points (0, −900) and (0, −200) indicated by the two stars. Each point in the gray dashed curves (c) and (d) possesses a constant distance product between the point and two stations (Jones, 2007). The distance product here, $r_{1q}r_{2q}$, is between (0, −900) or (0, −200) and the two station locations.

off-diagonal elements of the source-inversion model resolution matrix and model covariance matrix in the next example. We also image the diagonal and off-diagonal elements of MFP filter in the next example.

3.2. A Field-Array Example

3.2.1. Source Inversion

The array geometry (22 stations in Figure 2a) is adopted from a real array in Hartousov, Czech Republic, to monitor fumeroles (i.e., mofettes)—natural CO_2 leaks at the Earth's surface (e.g., Estrella et al., 2016). Based on the Rayleigh-wave phase velocities in this area, we use a 200 m/s phase velocity at 5 Hz. We use the same source grid as Xu et al. (2020), a 41-by-41 element grid with 5 m grid spacing on Earth's surface (i.e., the x–y plane). We pick two in-array and one outside array elements in the grid to aid our illustration of the model resolution and covariance (hypothetical sources 1, 2, and 3 in Figure 2a). Following the logic as in the previous example, we construct **A** using all 231 sensor pairs (Figures 2a and 2b). We apply SVD to **A** to calculate the model resolution and the diagonal elements of the covariance matrix for the source grid (Figures 2c and 2d). The model resolution is higher inside the array than outside the array. The resolution quantitatively indicates that this array configuration is not

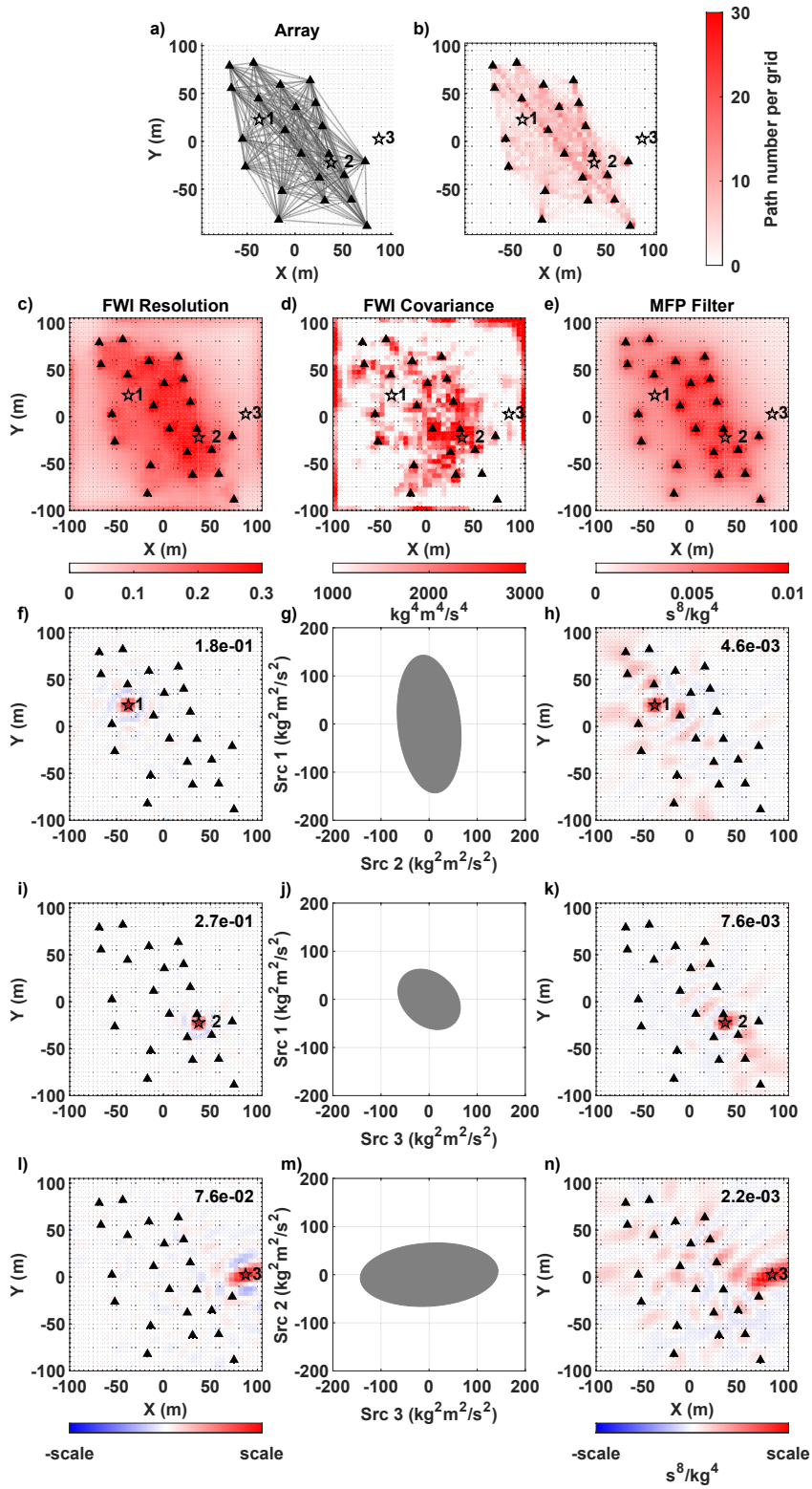

Figure 2. Illustration of the array geometry and the 231 sensor pairs (a), the sensor-pair-path number on each grid (b), the model resolution (c), and diagonal elements of the model covariance matrix (d) and the MFP filter (e) for the field array example. The black triangles are the stations. The gray lines in (a) are the 231 sensor pairs used in the example. The three empty black stars (1, 2, 3) are the three hypothetical sources used in illustration of the point spread functions from the model resolution (f), (i), (l), the trade-off between parameters (g), (j), (m), and the point spread functions from the MFP filter (h), (k), (n). In each point-spread-function subplot, we normalize the image with a scale, the absolute maximum value in the function, and the scale is in the top right-hand corner of the subplot.

sensitive to the four corners of the source grid. Inside the array, the resolution correlates with the sensor-pair path density (Figure 2b), and the high resolution is distributed where the sensor-pair paths are dense (e.g., hypothetical source 2 in Figure 2c). Besides of showing only the diagonal elements of the model resolution matrix, we also image the columns in the matrix to illustrate the point spread functions of individual grid nodes (Figures 2f, 2i, and 2l). For our hypothetical source locations 1, 2, and 3, the point spread functions possess high values at and around the hypothetical source locations. The point spread functions for the inside-array hypothetical sources (Figures 2f and 2i) are close to a spike function. However, the point spread function for the outside-array hypothetical source (Figure 2l) is far from a spike function due to no path coverage.

We observe that for the model covariance matrix, the diagonal elements possess high values, especially at the edges (Figure 2d). Note in this example, we have many small singular values (much less than 1, Figure 3a). Thus, the small singular values increase the covariance values through the $\mathbf{S}_P^{-2}$ term in calculation of model covariance matrix (Equation 7). Based on the model covariance matrix, we also demonstrate the trade-off through the 95% confidence ellipsoid for the parameter pairs between the three hypothetical sources (Figures 2g, 2j, 2m, and Appendix B). If a trade-off exists between two parameters, the ellipsoid is tilted off either the parameter axes (Figures 2g and 2j). Thus, one needs to consider the trade-off when interpreting the source inversion results.

To decrease the covariance values, we truncate the singular values to avoid the small singular values (much less than 1), which increase the covariance matrix values. For the source inversion with all 231 sensor pairs, we truncate the singular values at a threshold (i.e., 10% of the maximum singular value, Figure 3a) and then repeat the computation of the model resolution matrix and the model covariance matrix (Figures 3b and 3c, respectively). Compared to using all the singular values (Figure 2c), the model resolution no longer includes high values on the image edges (Figure 3b) and the point spread functions are still focused (Figures 3e, 3h, 3k). However, the truncation leads to decrease of both the resolution values and the peak values of the point spread functions. Meanwhile, due to the truncation, the diagonal element values of the model covariance matrix decrease (Figure 3c) and the confidence ellipse sizes are much smaller (Figures 3f, 3i, 3l), which indicate lower uncertainty and parameter trade-off in the source inversion. Although the truncated SVD brings these benefits, we need to notice that this approach is in fact a regularization for the source inversion (e.g., Aster et al., 2012). Therefore, the model resolution matrix and the model covariance matrix from the truncated SVD describe the regularized solution, not the true solution. We present another way to decrease the covariance matrix values without regularization in Section 4.1.

3.2.2. Comparison to MFP

We image the MFP filter (Section 2.4) to visualize the sensitivity of MFP to different sources. In the 231-sensor-pair example without truncation of singular values, we observe that the diagonal components (Figure 2e) correlate to the sensor-pair path density (Figure 2b), where the inside-array sources generally possess higher resolution than the outside-array sources. Inside the array, the filter values are heterogeneous and much less than 1. Furthermore the columns in the MFP filter provide the point spread functions corresponding to the three hypothetical sources (Figures 2h, 2k, 2n). We observe that the MFP filter blurs the true source strengths, no matter if the sources are in the array or outside array; furthermore, each source strength is blurred differently. The point spread functions of MFP are less focused than of the source inversion around the hypothetical sources (Figures 2f, 2i, 2l). This difference is because the MFP result inherently includes the array information (Equation 15).

We also apply the truncated SVD to the MFP filter (Equation 17). For the diagonal elements, we do not observe obvious changes from the truncation (Figure 3d); the scale values (absolute maximum values) in the MFP point spread functions are almost the same as before the truncation (Figures 3g, 3j, 3m). This is because the singular values contribute to MFP filter as the $\mathbf{S}_P^2$ term (Equation 17), and thus, the small singular values do not contribute much even before the truncation. Therefore, MFP is more robust to the small singular values than source inversion.

One needs to remove the MFP filter from the MFP results, in order to achieve the true source strength information like in monitoring the seismic source spatial-temporal changes (e.g., Gal et al., 2018). This removal is similar to the deconvolution of array response from seismic source backprojection results (e.g., Haney, 2014) or from surface wave dispersion estimates (e.g., Luo et al., 2008; Mikesell et al., 2017; Trad et al., 2003). However one can use MFP as a fast option to locate the seismic sources, since MFP only involves matrix multiplication and does not require inversion.

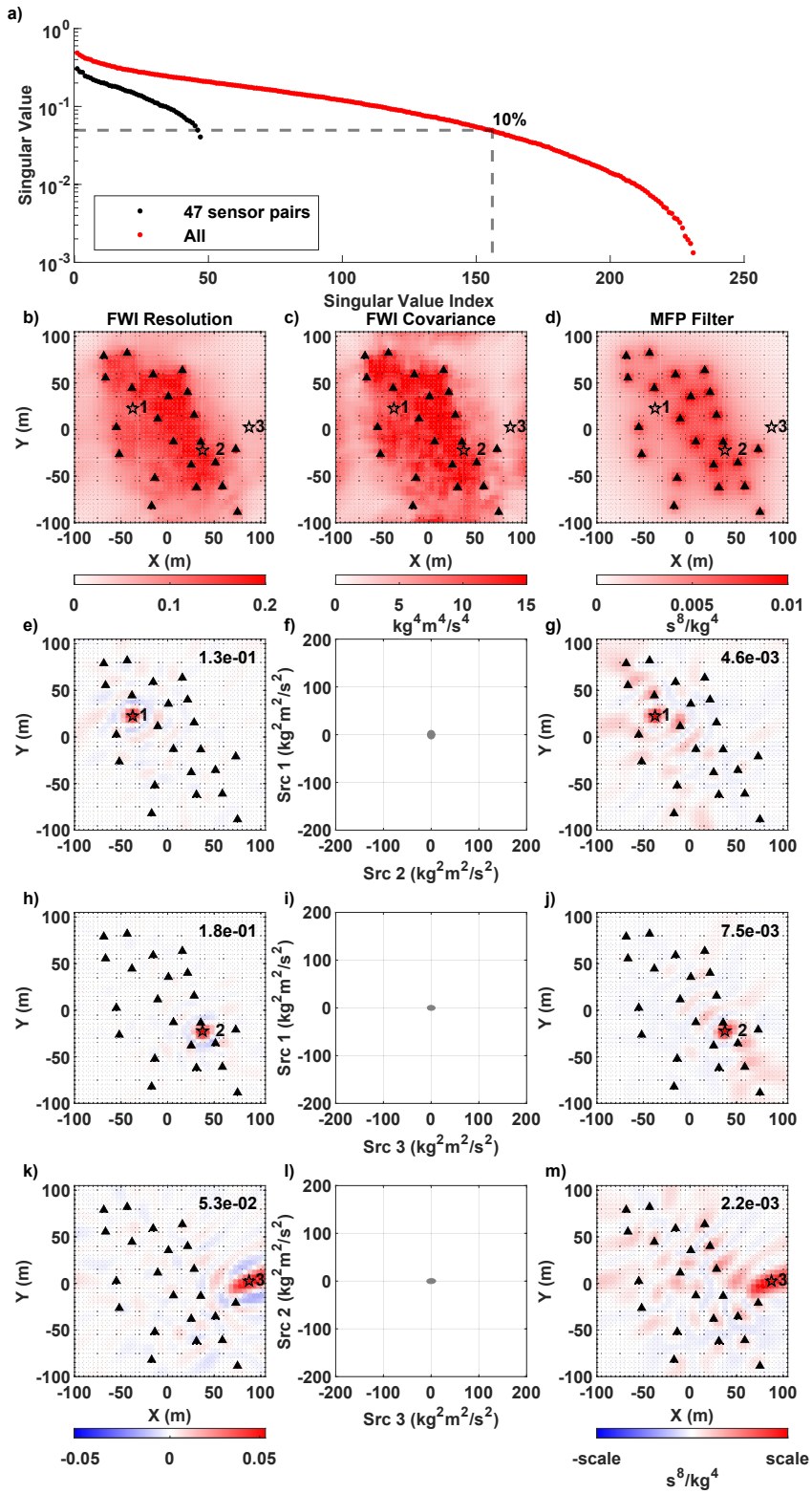

Figure 3. The model resolution and covariance for all the sensor pairs through the truncated SVD. (a) The singular values for all 231 sensor pairs (red dots, Figure 2) and the 47-sensor-pair example (black dots, Figure 4). The two gray dashed lines indicate the truncation location, the 156th singular value which is 10% of the largest singular value. All the calculation and figure settings for the resolution and covariance match those in Figure 2.

4. Discussion

To further our understanding even more, instead of using all the sensor pairs in the field array example, we choose a subset of the pairs to estimate the model resolution and covariance (Section 4.1). We then demonstrate the existence of the model null space in the different methods, for example, MFP and source inversion (Section 4.2). We finally discuss application of our analyze in the seismic array design (Section 4.3) and the limitation of our calculation of resolution and covariance (Section 4.4)

4.1. Winnowing Sensor Pairs

In practice, one winnows sensor pairs in an array to choose the crosscorrelations with high signal-to-noise ratio. We use 47 sensor pairs from the field array (Figure 4a) selected by Xu et al. (2020), where these sensor pairs sample the area heterogeneously (Figure 4b). For the source inversion with the 47 sensor pairs, we repeat the computation of the model resolution matrix and the covariance matrix. Compared to the 231-sensor-pair example (Figure 2c), the model resolution here no longer includes high values on the image edges (Figure 4c), but due to the rank deficiency in this example, the model resolution values decrease. Furthermore, all the point spread functions are far from a spike function, no matter if the hypothetical source is inside or outside of the array (Figures 4f, 4i, 4l). We notice that most of the singular values here are larger than the truncation threshold used in the 231-sensor-pair example (Figure 3a). Thus, the diagonal element values of the model covariance matrix decrease (Figure 4d). However, note that the diagonal elements provide underestimated uncertainties because of the trade-off among the parameters (e.g., Aster et al., 2012), especially between the hypothetical sources 2 and 3 (Figure 4m). We observe that the trade-offs among the hypothetical sources are different from the 231-sensor-pair example. Thus, one needs to recalculate the model resolution and covariance matrices if one changes the sensor pairs used in source inversion.

We also image the MFP filter using the 47 sensor pairs. Similar to the 231-sensor pair example, we also observe the correlation relationship between the diagonal elements and the sensor-pair path density (Figure 4e). The MFP point spread functions here (Figures 4h, 4k, 4n) blurs the true source strengths similarly to the source inversion (Figures 4f, 4i, 4l).

4.2. Null Space

We notice that we have only used a part (subspace) of the whole model space. The whole model space is of dimension Q, that is, the source number. Due to the rank of $\mathbf{A}$ (e.g., P and $P < Q$), $\mathbf{A}$ does not span the whole model space and thus a model null space exists. The model null space is spanned by the last $Q - P$ columns in $\mathbf{V}$ (Section 2.1). If we add any vectors (e.g., $\mathbf{x}_0$) in the model null space to the solutions for $\mathbf{A}$, the data fitting will not change (e.g., Aster et al., 2012), since

$$\mathbf{A}\mathbf{x}_0 = \mathbf{U}\mathbf{S}\mathbf{V}^{\dagger}\mathbf{x}_0 = \mathbf{U}\left[\mathbf{S}_P\,\mathbf{0}\right]\left[\mathbf{V}_P\,\mathbf{V}_{J-P}\right]^{\dagger}\mathbf{x}_0 = \mathbf{U}_P\mathbf{S}_P\mathbf{V}_P^{\dagger}\mathbf{x}_0 = 0, \tag{20}$$

where $\mathbf{x}_0$ is orthogonal to the row space spanned by $\mathbf{V}_P$ (e.g., Strang, 2016). Thus, a solution from solving $\mathbf{A}$ provides the same misfit as the combination of the solution and $\mathbf{x}_0$. If we incorporate the error in the observed data, the null space will be larger, which means even more solutions can satisfy the misfit between the synthetic and observation data within the error (e.g., Deal & Nolet, 1996; Fichtner, 2021). However, if we use multiple frequencies instead of one frequency, the model null space should be reduced.

The model null space also exists in the nonlinear source inversion. For the gradient descent algorithm, since the gradient is in the row space (Section 2.3), if the initial model is also in the row space, the model null space of the nonlinear source inversion is the same as the linear source inversion. Thus, if the initial model includes a part in the model null space, this part will not be changed during the updating (Claerbout, 2014, Chapter 2.3.4). Finally, note that the model null space also exists in MFP (Equation 18).

The model null space also exists for the misfit functions other than the L_2-norm waveform misfit (χ, e.g., envelope) in the nonlinear source inversion. We recognize that these misfit functions are functions of the synthetic waveforms (i.e., $\mathbf{b}$) of a trial solution. These misfit function values do not vary if we incorporate a vector ($\mathbf{x}_0$) from the linear-source-inversion model null space, since

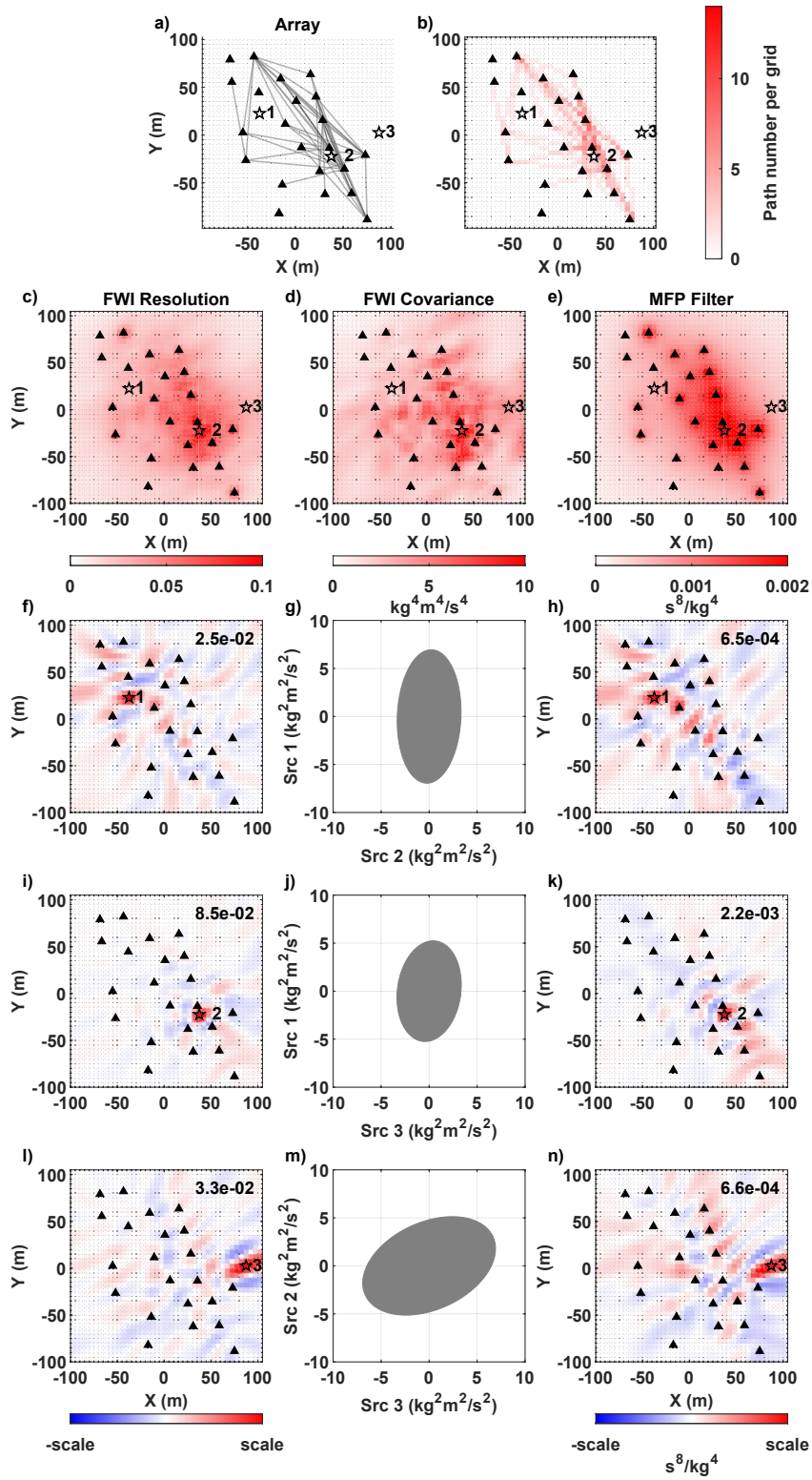

Figure 4. The model resolution, the model covariance, and the MFP filter for the 47 sensor pairs. All the calculation and figure settings match those in Figure 2.

$$\chi(\mathbf{b}) = \chi(\mathbf{b} + \mathbf{A}\mathbf{x}_0). \quad (21)$$

Therefore, the model null space for any misfit function includes the model null space of the linear source inversion. Note that we do not consider regularization of model parameters in the misfit function (e.g., Tikhonov regularization). Regularization leads to the misfit function directly depending on the model parameters and thus changes the model null space. Our analysis could be applied for a given regularization to determine the regularized solution resolution (Section 3.2.1).

4.3. Designing and Assessing a Seismic Array

Given that with the analysis presented, one can assess the resolution of an array for source distribution analysis, and the design of an observation array could be optimized. For example, if one plans to delineate an ambient seismic source spatial distribution (e.g., CO_2 fumaroles) and has the rough estimate of the source location and the subsurface velocity, one could use the analysis presented here to design an array that maximizes the model resolution around the estimated source locations. Meanwhile one could also apply this analysis to assess the resolution of an existing array to potential source locations.

4.4. Limitations in This Estimation

Our analysis above is based on SVD and only involves the array geometry and physics of the inversion. However in practice, one needs to consider the data errors if one plans to incorporate sensor pairs with different signal-to-noise ratios. For example, one can use the data standard deviation or the data covariance matrix to weight the data and **A** in the inversion (e.g., Aster et al., 2012). This incorporation would be especially necessary where the high signal-to-noise-ratio sensor pairs are not enough to constrain the inversion.

Our analysis can work for source inversion with low parameter numbers (around 10^3), for example, in near surface or urban environments. However, for inversions with large parameter numbers (e.g., $\geq 10^5$), the SVD in our analysis requires expensive computation cost. To minimize the parameter numbers, one can change the source grid from a homogeneous grid to a spatially variable grid (e.g., Igel et al., 2021) or adapt the grid size based on the model resolution (Section 3), for example, smaller/larger grids in the high/low-resolution areas. Another way to avoid the expensive computation cost is to estimate the model resolution and covariance using the Lanczos bidiagonalization (e.g., Yao et al., 1999; Zhang & Thurber, 2007).

Our estimation of the model resolution and covariance is based on the linear inversion or the nonlinear inversion with the waveform misfit function. However, for the nonlinear source inversion with other types of misfit functions (e.g., envelope), the Jacobian matrix is not exactly **A** and thus our estimation here may not always be applicable. In that case, to estimate the model resolution and covariance, one could utilize the Hessian matrix (e.g., Aster et al., 2012; Fichtner & Trampert, 2011b) or adopt the Monte Carlo algorithm (e.g., Tarantola, 2005).

5. Conclusion

We calculate the model resolution matrix and model covariance matrix for the ambient source inversion problem using linear inversion theory. The model resolution estimates, the diagonal elements of the resolution matrix, are generally higher inside than outside an array, and the inside-array resolution estimates are correlated with the sensor-pair path density. Meanwhile the columns (i.e., point spread functions) of the resolution matrix indicate the blurring effect of source inversion. We demonstrate that the model covariance matrix of the linear source inversion is the same as the nonlinear source inversion with the L_2-norm waveform misfit function. The covariance matrix provides uncertainty estimates and the trade-off among the sources. We also demonstrate that the results of matched field processing (MFP) are blurred by the MFP filter, and thus the model resolution of MFP is worse than source inversion when all sensor pairs are used in the field example. We finally demonstrate that the model null space for the linear source inversion also exists in MFP and the nonlinear source inversion. This research theoretically aids studies about estimation of the ambient seismic source distributions.

Appendix A: MFP Covariance

We write the covariance of the MFP estimate as.

$$\mathrm{Cov}(\mathbf{y}) = \mathbf{A}^{\dagger}\mathrm{Cov}(\mathbf{b})\mathbf{A}, \tag{A1}$$

$$= \sigma^2 \mathbf{V}_P \mathbf{S}_P^2 \mathbf{V}_P^{\dagger}, \tag{A2}$$

where we assume that the data errors are constant and independent among all crosscorrelations. Note that Equation A2 is identical to the MFP filter (Equation 17) if we further assume $\sigma = 1$.

Appendix B: Computation of Confidence Interval

We present a pseudocode for computation of the 95% confidence ellipsoid for two model parameters in an inversion problem. The computation is from Aster et al., 2012 Chapter 2.2 (Algorithm 1).

Algorithm 1. Computation of 95% confidence ellipsoid for two parameters

Input: covariance matrix ($\mathbf{C_m}$), the indexes for the two parameters (*ipa*, *ipb*)

theta = 0:0.01:2*pi ▷ All the angles along the ellipsoid

C = $\mathbf{C_m}$ ([ipa,ipb],[ipa,ipb]) ▷ Extract the covariance components corresponding to the two parameters

[u,lam] = eig(inv(C)); ▷ Compute eigenvectors and eigenvalues from the inverse of the extracted 2-by-2 matrix

F^{-1} = chi2inv(95%,2) ▷ 95th percentile of the χ^2 distribution with 2 parameters

semi_axes = sqrt(F^{-1}/diag(lam)) ▷ 95% confidence ellipsoid semiaxis lengths

x = semi_axes(1) * u(1,1) * cos(theta) + semi_axes(2) * u(1,2) * sin(theta) ▷ the x component for the ellipsoid

y = semi_axes(1) * u(2,1) * cos(theta) + semi_axes(2) * u(2,2) * sin(theta) ▷ the y component for the ellipsoid

Data Availability Statement

We use synthetic data and describe how to generate the synthetic data in the manuscript.

Acknowledgments
The authors thank R. Snieder for inspiring discussion about source inversion in September 2018. ZX thanks Jodi Mead for her inverse theory lectures. The authors thank editor Michael Bostock, associate editor Andreas Fichtner, and reviewers Jonas Igel and Laura Ermert for their constructive feedback that helped improve this manuscript. The authors also thank support from the National Science Foundation under Grant No. 1643795. ZX acknowledges support from the ANR MAGIS (ANR-19-CE31-0008-08).

References

Ardhuin, F., Gualtieri, L., & Stutzmann, E. (2015). How ocean waves rock the Earth: Two mechanisms explain microseisms with periods 3 to 300 s. *Geophysical Research Letters*, *42*(3), 765–772. https://doi.org/10.1002/2014gl062782

Aster, R. C., Borchers, B., & Thurber, C. H. (2012). *Parameter estimation and inverse problems*. Academic Press.

Ayala-Garcia, D., Curtis, A., & Branicki, M. (2021). Seismic interferometry from correlated noise sources. *Remote Sensing*, *13*(14), 2703. https://doi.org/10.3390/rs13142703

Baggeroer, A. B., Kuperman, W., & Schmidt, H. (1988). Matched field processing: Source localization in correlated noise as an optimum parameter estimation problem. *Journal of the Acoustical Society of America*, *83*(2), 571–587. https://doi.org/10.1121/1.396151

Bensen, G. D., Ritzwoller, M. H., Barmin, M. P., Levshin, A. L., Lin, F., Moschetti, M. P., et al. (2007). Processing seismic ambient noise data to obtain reliable broad-band surface wave dispersion measurements. *Geophysical Journal International*, *169*(3), 1239–1260. https://doi.org/10.1111/j.1365-246x.2007.03374.x

Bowden, D. C., Sager, K., Fichtner, A., & Chmiel, M. (2021). Connecting beamforming and kernel-based noise source inversion. *Geophysical Journal International*, *224*(3), 1607–1620.

Bozdağ, E., Trampert, J., & Tromp, J. (2011). Misfit functions for full waveform inversion based on instantaneous phase and envelope measurements. *Geophysical Journal International*, *185*(2), 845–870.

Brodsky, E. E., Gordeev, E., & Kanamori, H. (2003). Landslide basal friction as measured by seismic waves. *Geophysical Research Letters*, *30*(24). https://doi.org/10.1029/2003gl018485

Bucker, H. P. (1976). Use of calculated sound fields and matched-field detection to locate sound sources in shallow water. *Journal of the Acoustical Society of America*, *59*(2), 368–373. https://doi.org/10.1121/1.380872

Burtin, A., Vergne, J., Rivera, L., & Dubernet, P. (2010). Location of river-induced seismic signal from noise correlation functions. *Geophysical Journal International*, *182*(3), 1161–1173. https://doi.org/10.1111/j.1365-246x.2010.04701.x

Claerbout, J. (2014). *Geophysical image estimation by example*. Lulu. com.

Cros, E., Roux, P., Vandemeulebrouck, J., & Kedar, S. (2011). Locating hydrothermal acoustic sources at Old Faithful Geyser using matched field processing. *Geophysical Journal International*, *187*(1), 385–393. https://doi.org/10.1111/j.1365-246x.2011.05147.x

Datta, A., Hanasoge, S., & Goudswaard, J. (2019). Finite-frequency inversion of cross-correlation amplitudes for ambient noise source directivity estimation. *Journal of Geophysical Research: Solid Earth*, *124*(7), 6653–6665. https://doi.org/10.1029/2019jb017602

Deal, M. M., & Nolet, G. (1996). Nullspace shuttles. *Geophysical Journal International*, *124*(2), 372–380. https://doi.org/10.1111/j.1365-246x.1996.tb07027.x

Ermert, L., Sager, K., Afanasiev, M., Boehm, C., & Fichtner, A. (2017). Ambient seismic source inversion in a heterogeneous Earth-Theory and application to the Earth's hum. *Journal of Geophysical Research: Solid Earth*. https://doi.org/10.1002/2017jb014738

Ermert, L., Villaseñor, A., & Fichtner, A. (2015). Cross-correlation imaging of ambient noise sources. *Geophysical Journal International*, *204*(1), 347–364. https://doi.org/10.1093/gji/ggv460

Estrella, H. F., Umlauft, J., Schmidt, A., & Korn, M. (2016). Locating mofettes using seismic noise records from small dense arrays and matched field processing analysis in the NW Bohemia/Vogtland Region, Czech Republic. *Near Surface Geophysics*, *14*(4), 327–335.

Fichtner, A. (2014). Source and processing effects on noise correlations. *Geophysical Journal International*, *197*(3), 1527–1531. https://doi.org/10.1093/gji/ggu093

Fichtner, A. (2021). *Lecture notes on inverse theory*. Cambridge Open Engage.

Fichtner, A., Bowden, D., & Ermert, L. (2020). Optimal processing for seismic noise correlations. *Geophysical Journal International*, *223*(3), 1548–1564. https://doi.org/10.1093/gji/ggaa390

Fichtner, A., Kennett, B. L., Igel, H., & Bunge, H.-P. (2008). Theoretical background for continental-and global-scale full-waveform inversion in the time–frequency domain. *Geophysical Journal International*, *175*(2), 665–685. https://doi.org/10.1111/j.1365-246x.2008.03923.x

Fichtner, A., Stehly, L., Ermert, L., & Boehm, C. (2017). Generalised interferometry-I. Theory for inter-station correlations. *Geophysical Journal International*, *208*, 603–638. https://doi.org/10.1093/gji/ggw420

Fichtner, A., & Trampert, J. (2011a). Hessian kernels of seismic data functionals based upon adjoint techniques. *Geophysical Journal International*, *185*(2), 775–798. https://doi.org/10.1111/j.1365-246x.2011.04966.x

Fichtner, A., & Trampert, J. (2011b). Resolution analysis in full waveform inversion. *Geophysical Journal International*, *187*(3), 1604–1624. https://doi.org/10.1111/j.1365-246x.2011.05218.x

Gal, M., Reading, A., Rawlinson, N., & Schulte-Pelkum, V. (2018). Matched field processing of three-component seismic array data applied to Rayleigh and Love microseisms. *Journal of Geophysical Research: Solid Earth*, *123*(8), 6871–6889. https://doi.org/10.1029/2018jb015526

Grob, M., Maggi, A., & Stutzmann, E. (2011). Observations of the seasonality of the Antarctic microseismic signal, and its association to sea ice variability. *Geophysical Research Letters*, *38*(11). https://doi.org/10.1029/2011gl047525

Gualtieri, L., Bachmann, E., Simons, F. J., & Tromp, J. (2020). The origin of secondary microseism Love waves. *Proceedings of the National Academy of Sciences*, *117*(47), 29504–29511. https://doi.org/10.1073/pnas.2013806117

Hanasoge, S. M. (2014). Measurements and kernels for source-structure inversions in noise tomography. *Geophysical Journal International*, *196*(2), 971–985. https://doi.org/10.1093/gji/ggt411

Haney, M. M. (2014). Backprojection of volcanic tremor. *Geophysical Research Letters*, *41*(6), 1923–1928. https://doi.org/10.1002/2013gl058836

Haney, M. M., Mikesell, T. D., vanWijk, K., & Nakahara, H. (2012). Extension of the spatial autocorrelation (SPAC) method to mixed-component correlations of surface waves. *Geophysical Journal International*, *191*(1), 189–206. https://doi.org/10.1111/j.1365-246x.2012.05597.x

Hasselmann, K. (1963). A statistical analysis of the generation of microseisms. *Reviews of Geophysics*, *1*(2), 177–210. https://doi.org/10.1029/rg001i002p00177

Igel, J. K., Ermert, L. A., & Fichtner, A. (2021). Rapid finite-frequency microseismic noise source inversion at regional to global scales. *Geophysical Journal International*, *227*(1), 169–183. https://doi.org/10.1093/gji/ggab210

Jones, D. L. (2007). A collection of loci using two fixed points. *Missouri Journal of Mathematical Sciences*, *19*(2), 141–150. https://doi.org/10.4135/9781412976930.n9

Juretzek, C., & Hadziioannou, C. (2016). Where do ocean microseisms come from? A study of love-to-Rayleigh wave ratios. *Journal of Geophysical Research: Solid Earth*, *121*(9), 6741–6756. https://doi.org/10.1002/2016jb013017

Longuet-Higgins, M. S. (1950). A theory of the origin of microseisms. *Philosophical Transactions of the Royal Society of London - Series A: Mathematical and Physical Sciences*, *243*(857), 1–35.

Luo, Y., Xia, J., Miller, R. D., Xu, Y., Liu, J., & Liu, Q. (2008). Rayleigh-wave dispersive energy imaging using a high-resolution linear Radon transform. *Pure and Applied Geophysics*, *165*(5), 903–922. https://doi.org/10.1007/s00024-008-0338-4

Menke, W. (2012). *Geophysical data analysis: Discrete inverse theory: MATLAB edition* (Vol. 45). Academic press.

Meyers, P. M., Prestegard, T., Mandic, V., Tsai, V. C., Bowden, D. C., Matas, A., et al. (2021). A linear inversion approach to measuring the composition and directionality of the seismic noise field. *Remote Sensing*, *13*(16), 3097. https://doi.org/10.3390/rs13163097

Mikesell, T. D., Gribler, G., Xu, Z., & Haney, M. M. (2017). High-resolution dispersion images from deblurred MASW. In *SEG Technical Program Expanded Abstracts 2017* (pp. 5284–5288). Society of Exploration Geophysicists. https://doi.org/10.1190/segam2017-17650859.1

Nishida, K., Kawakatsu, H., Fukao, Y., & Obara, K. (2008). Background Love and Rayleigh waves simultaneously generated at the Pacific Ocean floors. *Geophysical Research Letters*, *35*(16). https://doi.org/10.1029/2008gl034753

Retailleau, L., & Gualtieri, L. (2019). Toward high-resolution period-dependent seismic monitoring of tropical cyclones. *Geophysical Research Letters*, *46*(3), 1329–1337. https://doi.org/10.1029/2018gl080785

Roth, D. L., Finnegan, N. J., Brodsky, E. E., Cook, K., Stark, C., & Wang, H. (2014). Migration of a coarse fluvial sediment pulse detected by hysteresis in bedload generated seismic waves. *Earth and Planetary Science Letters*, *404*, 144–153. https://doi.org/10.1016/j.epsl.2014.07.019

Sager, K., Ermert, L., Boehm, C., & Fichtner, A. (2018). Towards full waveform ambient noise inversion. *Geophysical Journal International*, *212*(1), 566–590. https://doi.org/10.1093/gji/ggx429

Strang, G. (2016). *Introduction to linear algebra* (Vol. 5). Wellesley-Cambridge Press.

Tarantola, A. (2005). *Inverse problem theory and methods for model parameter estimation*. *Society for Industrial and Applied Mathematics*, (Vol. 89). SIAM.

Trad, D., Ulrych, T., & Sacchi, M. (2003). Latest views of the sparse Radon transform. *Geophysics*, *68*(1), 386–399. https://doi.org/10.1190/1.1543224

Tromp, J., Luo, Y., Hanasoge, S., & Peter, D. (2010). Noise cross-correlation sensitivity kernels. *Geophysical Journal International*, *183*(2), 791–819. https://doi.org/10.1111/j.1365-246x.2010.04721.x

Tsai, V. C., Minchew, B., Lamb, M. P., & Ampuero, J.-P. (2012). A physical model for seismic noise generation from sediment transport in rivers. *Geophysical Research Letters*, *39*(2). https://doi.org/10.1029/2011gl050255

Umlauft, J., & Korn, M. (2019). 3-D fluid channel location from noise tremors using matched field processing. *Geophysical Journal International*, *219*(3), 1550–1561. https://doi.org/10.1093/gji/ggz385

Umlauft, J., Lindner, F., Roux, P., Mikesell, T. D., Haney, M. M., Korn, M., & Walter, F. T. (2021). Stick-slip tremor beneath an alpine glacier. *Geophysical Research Letters*, *48*(2), e2020GL090528. https://doi.org/10.1029/2020gl090528

Wapenaar, K., & Fokkema, J. (2006). Green's function representations for seismic interferometry. *Geophysics*, *71*(4), SI33–SI46. https://doi.org/10.1190/1.2213955

Xu, Z., Mikesell, T. D., Gribler, G., & Mordret, A. (2019). Rayleigh-wave multicomponent cross-correlation-based source strength distribution inversion. Part 1: Theory and numerical examples. *Geophysical Journal International*, *218*(3), 1761–1780. https://doi.org/10.1093/gji/ggz261

Xu, Z., Mikesell, T. D., Umlauft, J., & Gribler, G. (2020). Rayleigh-wave multicomponent crosscorrelation-based source strength distribution inversions. Part 2: A workflow for field seismic data. *Geophysical Journal International*, *222*(3), 2084–2101. https://doi.org/10.1093/gji/ggaa284

Yao, Z., Roberts, R., & Tryggvason, A. (1999). Calculating resolution and covariance matrices for seismic tomography with the LSQR method. *Geophysical Journal International*, *138*(3), 886–894. https://doi.org/10.1046/j.1365-246x.1999.00925.x

Zhang, H., & Thurber, C. (2007). Estimating the model resolution matrix for large seismic tomography problems based on Lanczos bidiagonalization with partial reorthogonalization. *Geophysical Journal International*, *170*(1), 337–345. https://doi.org/10.1111/j.1365-246x.2007.03418.x